Journal of Materials Research and Technology 36 (2025) 5286–5297

Contents lists available at ScienceDirect

Journal of Materials Research and Technology

journal homepage: www.elsevier.com/locate/jmrt

Microbiologically influenced corrosion of Al–Cu–Li alloy by *Pseudomonas aeruginosa*

C.G. Ramírez [a,b,*], A. Monsalve [b], C. Montero [c], J. Espinoza [a], J. Araujo [d], N. Vejar [e], M. Azócar [a], M. Gulppi [a], V.M. Jiménez-Arevalo [a], X. Zhou [f], M.A. Páez [a,**]

[a] Departamento de Química de los Materiales, Facultad de Química y Biología, Universidad de Santiago, Av. L. B. O'Higgins, 3363, Santiago, Chile
[b] Departamento de Ingeniería metalúrgica, Facultad de ingeniería, Universidad de Santiago de Chile, Av. L. B. O'Higgins, Casilla 40, Correo 33, 3363, Santiago, Chile
[c] Instituto de Química, Facultad de Ciencias, Universidad católica de Valparaíso, Avenida Universidad 8 330, Placilla, Valparaíso, Chile
[d] Instituto de Pesquisas Energéticas e Nucleares, IPEN/CNEN, Av. Prof. Lineu Prestes, 2242, São Paulo, Brazil
[e] Centro de Investigación y Desarrollo en Ciencias Aeroespaciales, Fuerza Aérea de Chile, Av. José Miguel Carrera, 11087, Santiago, Chile
[f] Department of Materials, University of Manchester, Oxford Road, M13 9PL, Manchester, United Kingdom

ARTICLE INFO

Handling editor: M Meyers

Keywords:
Microbiologically influenced corrosion
Al–Cu–Li alloy
Localized corrosion
Biofilms
Pseudomonas aeruginosa
Cross-sectional analysis

ABSTRACT

This study investigates microbiologically influenced corrosion (MIC) of the Al–Cu–Li alloy AA2060-T8 caused by *Pseudomonas aeruginosa*. Key parameters—bacterial population (OD_{600}), specific biofilm-forming capacity (SBF), pH, and open circuit potential (OCP)—were monitored over time and correlated with bacterial growth stages. A colonization time range between 3 and 10 h was identified (OD_{600}: 0.23–0.67), during which *P. aeruginosa* produced a critical biofilm amount (SBF: 0.14–0.74) sufficient to sustain irreversible adhesion on the alloy surface, as indicated by the OCP increase from 4 h. Furthermore, a pH decrease from 7.6 to 6.8 was observed during the exponential stage, likely reaching pH 3.5–4.5 within colony cores. This could have created conditions that facilitated the destabilization of the oxide layer beneath the biofilm, making the alloy more susceptible to localized corrosion. After 24 h of exposure to the MIC testing solution, cross-sectional analysis of the alloy revealed discontinuities within the biofilm, which allowed the electrolyte to reach the alloy surface and promote the formation of local differential cells. Thus, MIC of the AA2060-T8 alloy caused by *P. aeruginosa* is mainly due to the combined effects of pH decrease and the formation of discontinuities acting as channels within the biofilm. These findings provide new insights into the MIC of Al–Cu–Li alloys, paving the way for future protection strategies against MIC.

1. Introduction

The relevance of Al–Cu alloys in modern aircraft and spacecraft applications lies in their low cost, lightweight properties, and high specific strength [1]. Given the exponential growth of these industries and the increasingly strict environmental regulations aimed at reducing CO_2 emissions, optimizing energy efficiency through the adoption of sustainable fuels and advanced lightweight materials has become a critical objective for the coming years [2]. Since aluminum alloys constitute 60–80 % of the total weight of a typical commercial aircraft [3], an effective strategy for improving energy efficiency and increasing payload capacity is to reduce the density of Al–Cu alloys by incorporating lithium (Li), which has an exceptionally low density of 0.54 g/cm^3. It has been shown that adding 1 % lithium reduces alloy density by 3 % and increases the Young modulus by about 6 % [4]. These improvements offer clear advantages for structural applications in fuselage, ailerons, and internal parts of modern aircraft [5] and spacecraft [6]. Given these characteristics, third-generation Al–Cu–Li alloys such as the AA2060-T8 series have been increasingly adopted in the aerospace industry over the last decade [7].

Despite the numerous advantages of Al–Cu–Li alloys, their applications still face challenges in coastal and marine environments because of their susceptibility to localized corrosion under high humidity and salinity conditions. Several studies have examined the corrosion behavior of Al–Cu–Li alloys in sodium chloride solutions, establishing a strong correlation between the Al matrix and T_1 hardening phase [4,8,

* Corresponding author.
** Corresponding author.
E-mail addresses: cristian.ramirez.f@usach.cl (C.G. Ramírez), maritza.paez@usach.cl (M.A. Páez).

https://doi.org/10.1016/j.jmrt.2025.04.188
Received 1 February 2025; Received in revised form 6 April 2025; Accepted 17 April 2025
Available online 19 April 2025

9]. The T_1 phase, composed of Al_2CuLi, acts as a cathodic site inducing localized corrosion and subsequent matrix degradation via a dealloying process [10]. This high susceptibility of the T_1 phase to initiating localized corrosion under saline conditions, such as those in coastal environments, promotes the formation of microscopic differential cells near these intermetallic precipitates. However, most studies on the corrosion behavior of Al–Cu–Li alloys have focused exclusively on abiotic environments, leaving a significant gap in understanding their performance in the presence of microorganisms, which are well known to cause microbiologically influenced corrosion (MIC) [11].

Among the most common MIC mechanisms are bacterial extracellular electron transfer (EET) and the production of corrosive metabolites. EET involves metal-to-microbe electron transfer, where bacteria utilize the metal as an electron donor and a non-oxygenated oxidant (such as sulfate or nitrate) as an acceptor, thereby facilitating corrosion [12,13]. On the other hand, the production of corrosive metabolites is mainly associated with acid metabolites formed during bacterial growth, which can create an aggressive environment that accelerates material degradation [14,15]. Both mechanisms are closely related to bacterial metabolic activity. However, MIC in aluminum alloys mainly results from passive layer destabilization and heterogeneous biofilm formation driven by microbial colonization.

In particular, biofilm-forming bacteria such as *Pseudomonas* have been identified as significant risk factor to the integrity of traditional Al–Cu alloys [15–18]. Among its species, *Pseudomonas aeruginosa* has been frequently used as a model microorganism to study MIC in aerospace structures [19,20]. This Gram-negative, facultative aerobic bacterium can grow under diverse environmental conditions, including temperatures between 25 and 37 °C and a broad range of nutrient media [21]. One of the main characteristics of *P. aeruginosa* is its high capacity to produce extracellular polymeric substances (EPS), which promote the formation of heterogeneous biofilms that facilitate microbial adhesion to metal surfaces.

In the context of MIC in Al–Cu alloys, these biofilms can play several roles at the metal–solution interface, including modification of the transport of chemical species toward the metal surface [22], enhancement of biofilm adhesion to aluminum via direct interaction of carboxylic and phosphoryl functional groups in mature biofilms [15], disruption of the protective properties of the native alumina oxide layer [17], and initiation of localized corrosion driven by differential aeration cells associated with the heterogeneous distribution of the biofilm [23].

Although representative schemes of differential aeration cells induced by biofilms on Al–Cu alloys have been previously proposed [18], there is no direct cross-sectional evidence of these zones beneath the biofilm in the literature. Furthermore, a thorough literature review revealed that studies specifically addressing MIC in Al–Cu–Li alloys are scarce, leaving fundamental questions unanswered. For instance, what is the correlation between the different stages of bacterial growth and biofilm formation on Al–Cu–Li alloy surfaces? Moreover, how does this biofilm influence the formation of differential cells and localized corrosion on Al–Cu–Li alloys?

To address these gaps, this study investigates the MIC processes induced by *P. aeruginosa* biofilm on the surface of the AA2060-T8 Al–Cu–Li alloy. Key parameters providing real-time insights during bacterial growth stages were measured, including pH, bacterial population through optical density (OD_{600}), specific biofilm-forming capacity (SBF), and open circuit potential (OCP). These measurements were utilized to correlate the distinct bacterial growth stages with the biofilm-forming capacity and biofilm adherence to the AA2060-T8 alloy over time. Cross-sectional analysis (SEM-EDS) revealed heterogeneous biofilms with channels allowing direct electrolyte-metal interactions, leading to localized corrosion beneath the biofilm. The corrosion currents of AA2060-T8 samples exposed to *P. aeruginosa* for 40 h were nearly four times higher than those observed in the sterile controls. These results underscore the role of heterogeneous biofilms in MIC, providing direct evidence of the differential zones beneath the biofilm and their contribution to localized corrosion in Al–Cu–Li alloys.

2. Materials and methods

2.1. Metal samples

The elemental composition of AA2060-T8 Al–Cu–Li alloy used in this study is listed in Table 1. For all electrochemical experiments, these samples were resized into plates with dimensions of 60x25x2 mm. All samples were subjected to a polishing process from 800 to 4000 grade SiC paper, using an automatic polisher and cold ethanol as a coolant. Then, each specimen was degreased with acetone, sonicated for 5 min in cold Milli-Q water to remove the solid particles from the mechanical polishing, dried and subsequently stored in a desiccator. Before the microbiological experiments, the samples were sterilized using germicide light (254 nm) for 15 min in a laminar flow chamber [24].

2.2. SEM-EDS analysis

For metallographic analysis, the specimens were polished with 0.04 μm alumina, etched with Keller solution for 30 s [25], and observed using an optical microscope. To preserve the integrity of the adhered biofilm, the samples were removed from the MHCl medium at different exposure times, gently rinsed three times by immersion in distilled water to eliminate non-adherent biofilm and stored in a sterile vacuum desiccator. To maintain the biofilm and corrosion products attached on the surface during cross-sectional cutting, samples were embedded in epoxy resin, resized, and then sectioned using a Leica EMUC7 ultramicrotome with a diamond knife. All samples were coated with a 20 nm carbon layer and analyzed with scanning electron microscopy (SEM) and energy dispersive X-ray spectroscopy (EDS) using a Quanta 650 instrument. For transmission electron microscopy (TEM), Al–Cu–Li samples were prepared by polishing 3 mm discs of AA2060-T8 alloy to a thickness of 20 μm, followed by twin-jet electropolishing at 15 V in a solution of HNO_3 and MeOH (1:3) at −20 °C. TEM analysis was then performed using an FEI Talos F200A instrument operated at 200 kV.

2.3. Microorganisms and culture medium

The sterile culture medium, referred to as MHCl medium, contained 1.25 wt% Mueller Hinton (MERCK) and 0.85 wt% NaCl (MERCK). The wild-type marine bacterium *P. aeruginosa* was used in this study. The *P. aeruginosa* stock was prepared by reactivating strains stored at −20 °C on Mueller Hinton Agar plates and incubating a single colony in MHCl medium at 37 ± 1 °C for 24 h. The resulting stock was stored at 4 °C. To activate the bacterial metabolism before experiments, 9 mL of MHCl medium was inoculated with 1 mL of the *P. aeruginosa* stock in a Falcon tube, then incubated on an orbital shaker at 37 ± 1 °C and 100 rpm for 24 h. This activated culture, designated as M1, was prepared 24 h before each experiment. All experiments were conducted with approximately one-third of the total volume left as headspace. All spectrophotometric measurements were performed using a Multiskan GO (Thermo Scientific). A bacterial growth time from 0 to 40h was selected to clearly identify the plateau in the stationary growth stage.

2.4. Bacterial growth assessment

To determine the bacterial growth under aerobic conditions at 25 °C, 180 μL of sterile MHCl was inoculated with 20 μL of M1 in 96-well polystyrene plates to achieve an initial concentration of 10^5 Colony Forming Units per mL (CFU/mL) of *P. aeruginosa*. The optical density (OD_{600}) was measured with 6 replicates for the MHCl with *P. aeruginosa* and 6 replicates for the MHCl sterile control every 1 h, up to 40 h.

Table 1
Elemental composition of AA2060-T8 alloy used in this study.

Element	Cu	Li	Mg	Zn	Ag	Mn	Si	Al
Composition (%wt.)	3.76	0.75	0.72	0.28	0.34	0.30	0.02	Balance

2.5. Specific biofilm formation assessment

Biofilm formation was measured by crystal violet staining of the 96-well polystyrene plates. The experimental design and methodology followed the guidelines and recommendations of Allkja et al. to ensure reproducibility and clarity in the evaluation of biofilm formation [26]. Multichannel micropipettes were used to prevent biofilm detachment during extraction and filling, ensuring that there was no contact with the sides or bottoms of the wells. Specific biofilm formation (SBF) values were determined using an adapted methodology from Niu et al. [27]. Data for each SBF curve point were collected from an independent set of 12 wells (6 positive controls and 6 negative controls), with each set incubated at 25 °C for intervals between 0 and 40 h to generate a full curve. The SBF curve presented in this study represents the average of three independently replicated curves conducted over different weeks (N = 3).

2.6. pH measurements

A set of Falcon tubes containing MHCl medium was inoculated with M1 to reach an initial concentration of 10^5 Colony Forming Units per mL (CFU/mL). Additionally, another set of tubes was prepared, each with an AA2060-T8 alloy piece (1 cm^2 of exposed area) immersed in MHCl medium. pH measurements were recorded inside the tubes every 2 h over a 40-h period. To prevent cross-contamination, independent single-use tubes were used for each pH reading. All measurements were performed in triplicate at 25 °C, with their respective sterile controls.

2.7. Electrochemical assessment

A Gamry electrochemical cell PTC1™ with a three-electrode configuration was used: a platinum counter electrode (CE), a saturated calomel reference electrode (RE), and the AA2060-T8 alloy as the working electrode (WE) positioned horizontally at the bottom of the cell with 1 cm^2 of exposed area. Before each experiment, all materials were sterilized in an autoclave, except for the electrodes, which were sterilized with 70 % EtOH and germicidal light (254 nm). The electrochemical cell was assembled inside a sterile laminar flow hood using 60 mL of inoculated MHCl medium (10^5 CFU/mL), then transferred to an incubator at 25 °C. Electrochemical measurements were performed in triplicate with their respective MHCl sterile controls. The open circuit potential (OCP) was recorded every hour from 0 to 40 h. Samples were removed, carefully rinsed with distilled water without any additives (such as surfactants) to avoid altering the surface's chemical composition, and stored in a sterile vacuum desiccator. Potentiodynamic polarization curves were obtained in a 0.85 % NaCl solution at a scan rate of 0.2 mV/s. The E/I curves were recorded in the anodic direction, up to +0.1 V vs. OCP, and in the cathodic direction, up to −0.1 V vs. OCP, using independent samples for each sweep. The ex-situ methodology allowed for the removal of non-adherent biofilm decanted by gravity onto the metal surface, ensuring that only firmly adhered biofilm remained, thus providing more representative measurements.

3. Results and discussion

3.1. Microstructure characterization

The grain distribution in Al–Cu–Li alloys strongly influences their corrosion susceptibility [28]. Fig. 1 presents the microstructure of the AA2060-T8 alloy, where differences in brightness correspond to a non-uniform distribution of crystallographic grain orientations, with darker areas indicating regions more susceptible to metallographic attack.

The microstructure of the AA2060-T8 alloy exhibits elongated grains aligned with the rolling direction (Fig. 1b), along with a heterogeneous distribution of grain dimensions in both short and long section views (Fig. 1a and 1c). The average aspect ratio (length/width) was 18.47, with most values ranging from 15 to 20 (Fig. 1c). This morphology results from the T8 heat treatment process, which includes solution treatment, cold deformation and artificial aging to optimize mechanical performance, such as load-bearing capacity and buckling resistance for aerospace applications. Additionally, this heat treatment promotes the

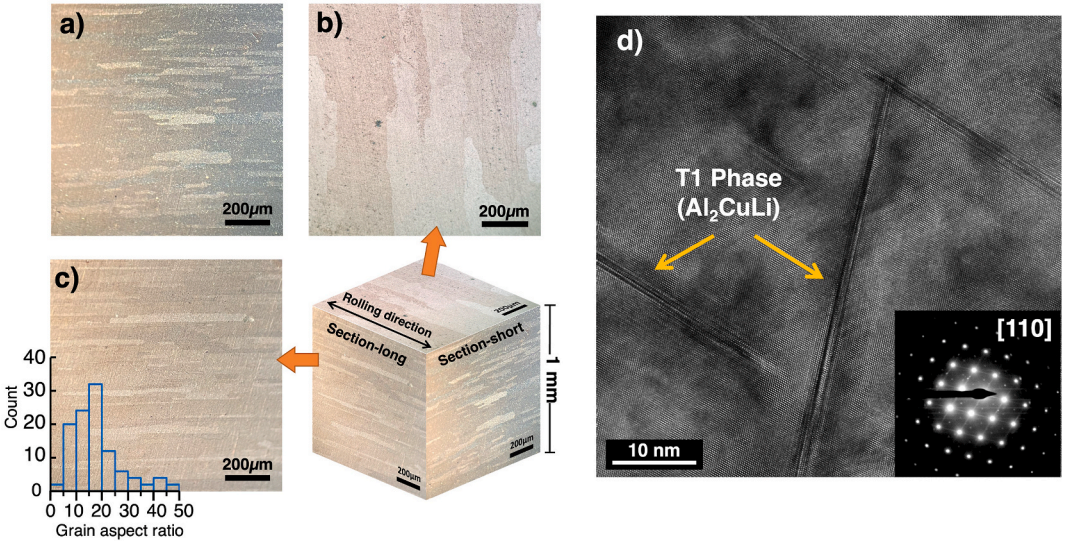

Fig. 1. Microstructure of AA2060-T8 alloy: (a) cross section-short transverse, (b) rolling surface, (c) cross section-long transverse and grain aspect ratio distribution, and (d) TEM image showing the T1 phase morphology and Selected Area Electron Diffraction (SAED) patterns from Al matrix in the AA2060-T8 alloy.

precipitation of intermetallic T_1 (Al_2CuLi) phases. TEM analysis (Fig. 1d) reveals the T_1 phase morphology, which nucleates and grows along the {111}Al planes of the α-Al matrix, both within grains and at grain boundaries during the artificial aging process [9]. The T_1 phase serves as strengthening phase in Al–Cu–Li alloys, forming uniformly distributed precipitates that act as obstacles to dislocation motion, increasing the critical resolved shear stress for slip deformation on crystal planes, and limiting plastic deformation [29]. Despite these mechanical enhancements, the T_1 phase is prone to localized corrosion and acts as a preferential corrosion site due to its cathodic behavior relative to the α-aluminum matrix, leading to crystallographic corrosion [8,9]. The susceptibility of the T1 phase to initiate localized corrosion arises from a phenomenon known as the "Nobility Switch," as reported by Jiang et al. [10]. In the first stage, the selective dissolution of Li from the T_1 (Al_2CuLi) phase occurs. This causes an inversion of the "Al_2CuLi (anodic)//α-Al matrix (cathodic)" electrochemical couple to a second pair, "Al_2Cu (cathodic)//α-Al matrix (anodic)". In the second stage, the local copper-rich remnant (Al_2Cu) formed during this 'Nobility Switch' acts as a cathodic site on the surface, promoting the propagation of corrosion along the {111}α planes of the aluminum matrix (FCC). This dealloying process culminates in a third stage, where "Cu° (cathodic)//α-Al matrix (anodic) is formed, driving the localized pitting corrosion around the Cu° deposit.

Li et al. reported that localized corrosion in Al–Cu–Li alloys preferentially initiates at intermetallic phases, promoting their dissolution and formation of corrosion products, which can induce modifications in surface morphology [30]. On the other hand, Yasmine et al. indicated that surface roughness influences the energy barrier that bacterial cells must overcome to reach the substrate surface, decreasing as asperity size increases [31]. Considering the high reactivity of the T1 phase, it is likely that the surface morphology of the AA2060-T8 alloy undergoes dynamic changes during immersion in the MHCl medium, increasing its roughness and consequently promoting biofilm adhesion. Furthermore, it has been reported that the preferential dissolution of the T1 phase leads to a localized corrosive environment with low pH [32]. Therefore, the Nobility switch process may be driven not only by potential differences but also by pH changes during the corrosion process. Consequently, the pH changes (Fig. 2b) associated with the bacterial metabolism could play a critical role in the MIC process observed in this study.

3.2. Evolution of key parameters during bacterial growth stages

Key parameters providing real-time insights into the biofilm forming process were measured during bacterial growth stages. The Optical density (OD_{600}) reflects the bacterial population while specific biofilm formation (SBF) quantifies the biofilm-forming capacity under specific conditions [27]. Because of its capacity to produce acidic metabolites [33], pH serves as a simple indicator for evaluating the metabolic activity of *P. aeruginosa*, whereas the open circuit potential (OCP) tracks the processes of biofilm formation and accumulation on the metallic surface [34]. Fig. 2 integrates the data obtained, illustrating the evolution of bacterial growth and biofilm formation on the AA2060-T8 Al–Cu–Li alloy exposed to MHCl with *P. aeruginosa*.

3.2.1. Bacterial growth and biofilm formation assessment

The growth kinetics of *P. aeruginosa* was measured at 25 °C (Fig. 2a, left axis), exhibiting the three characteristic stages of bacterial growth. The lag stage (0–2 h), defined by low OD_{600} values, represented the cellular adaptation and minimal proliferation. After 2 h, the increase in OD_{600} values represents the beginning of the exponential growth stage, marked by intensified nutrient consumption and optimal metabolic activity [11]. During this stage, *P. aeruginosa* increases the production of EPS, which provides structural integrity to the biofilm and facilitates the establishment of bacterial colonies on the Al–Cu–Li alloy surface. Finally, the bacterial population reaches a stationary stage (20–40 h),

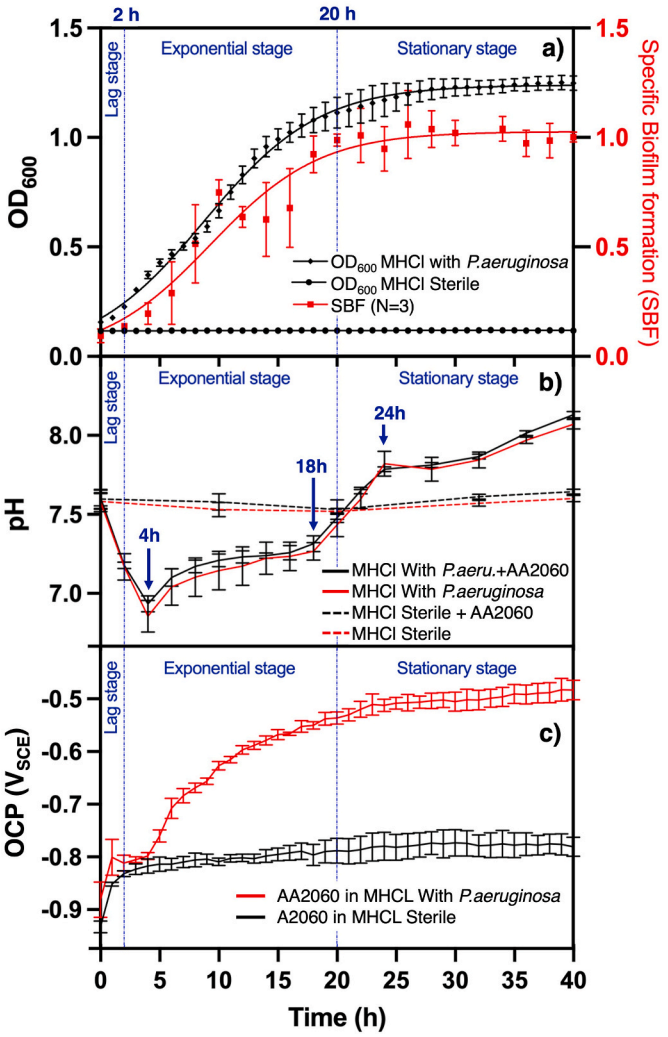

Fig. 2. Parameters measured during bacterial growth and biofilm formation on AA2060-T8 alloy: (a) Overlay of *P. aeruginosa* growth kinetics (OD_{600}, left axis) and specific biofilm formation (SBF, right axis) in MHCl medium at 25 °C (b) pH of the MHCl medium. (c) Open circuit potential (OCP) of the alloy.

characterized by a dynamic equilibrium between cell growth and death, primarily due to nutrient limitations. A similar behavior was described by Pellé et al., who associated the growth stages of *P. aeruginosa* with the Specific Biofilm Formation (SBF) over time [34]. During these stages, the SBF parameter can be calculated using Equation (1), as reported by Niu & Gilbert. [27], According to the authors, AB represents the absorbance of the crystal violet dye incorporated by the bacteria adhered to the biofilm, CW represents the control samples that account for dye adhered to the plates due to abiotic factors, and G is the optical density (OD_{600}) of the medium at each time point.

$$SBF = (AB - CW)/G \quad (1)$$

The bacterial population (OD_{600}) measured between 2 and 10 h ranged from 0.20 to 0.66 (Fig. 2a, left axis). These values represent the transition from the lag stage to the exponential growth stage and consequently indicate a weak biofilm-forming capacity (Table 2). When the G value in Equation (1) was substituted for these OD_{600} values, a multiplier effect ranging from 5 to 1.5 resulted in the AB−CW term, leading to SBF values greater than 1. According to Table 2, these SBF values would suggest a strong biofilm-forming capacity. However, at this transition point (2–10 h), the bacteria have not yet reached their optimal metabolic activity. As a result, Equation (1) may lead to misinterpretation when evaluating the initial hours of biofilm

Table 2
Semi-quantitative scale describing the biofilm-forming capacity of *P. aeruginosa* associated with its SBF values and bacterial growth stages.

Time range (h)	Measured OD_{600}	Measured SBF	SBF Range (Naves et al.)	biofilm-forming capacity	Bacterial growth stage
0–2	0.15 - 0.20	0.09 - 0.14	<0.3	Very weak	Lag
2–10	0.20 - 0.66	0.14–0.74*	0.3 - 0.7	Weak	Exponential (early)
10–20	0.66 - 1.11	0.74–0.98	0.7 - 1.0	Moderate	Exponential (late)
20–40	1.11 - 1.25	0.98–1.02	>1.0	Strong	Stationary

To simplify the analysis, the value (*) was classified within the '2–10' h range.

formation. Therefore, a modification of the SBF Equation (1) is proposed in Equation (2), where G_{stat} was set as a constant value ($G_{stat} = 1.2$), measured during the stationary stage. All SBF values shown in Fig. 2a were calculated every 2 h using Equation (2).

$$SBF = (AB - CW)/G_{stat}, \quad (2)$$

Based on the semi-quantitative scale of biofilm-forming capacity reported by Naves et al. [35], the SBF values obtained in this study were correlated with each bacterial growth stage and its corresponding biofilm-forming capacity (Table 2).

According to Table 2, the SBF values obtained during the lag stage revealed a very weak biofilm-forming capacity, associated with an insufficient bacterial population to produce substantial EPS. However, in the exponential stage, EPS production increases sufficiently to achieve irreversible adhesion on the surface, leading to biofilm formation. Finally, SBF stabilized at a plateau during the stationary stage, establishing a clear correlation between the bacterial growth stages and biofilm formation capacity over time. The maximum SBF value during the stationary growth stage was 1.02 (Table 2). Therefore, *P. aeruginosa* exhibits a strong biofilm-forming capacity, highlighting its ability to produce and accumulate biofilm on the surface of the AA2060-T8 alloy.

3.2.2. *pH measurement during bacterial growth*

Fig. 2b illustrates the pH changes in the MHCl medium across the bacterial growth stages. In the sterile MHCl medium, the pH remained stable over 40 h; however, significant fluctuations were observed in the MHCl medium with *P. aeruginosa*. Between 0 and 4 h, the pH decreased from 7.6 to 6.8, which was attributed to increased bacterial activity during the onset of exponential growth. As expected, the pH changes observed during bacterial growth were similar in the MHCl medium with and without the AA2060-T8 alloy, as the pH measurements were taken from the overall solution.

According to pH-Potential diagram for aluminum [36], this pH drop should not be enough to dissolve aluminum oxides or hydroxides into Al^{3+}. However, the localized pH microenvironments within the biofilms may differ significantly. Hollmann et al. analyzed real-time three-dimensional pH variations in *P. aeruginosa* biofilms, reporting a highly acidic environment within the core of the colonies (~pH 3.5–4.5), whereas the outer edges of these colonies exhibited a slightly acidic pH (5.5–6.0) [14]. According to the pH-Potential diagram, a pH below 4 can dissolve the aluminum oxide layer on the AA2060-T8 alloy. In line with this, Ghanbari et al. reported that the breakdown potential—the critical potential at which the protective oxide layer fails—of the AA2098-T8 Al–Cu–Li alloy in 0.1 M NaCl decreases linearly as pH decreases from 6.5 to 4.5 [37]. Consequently, the local pH values beneath the biofilm may have been sufficient to promote the dissolution of aluminum oxide. This interpretation aligns with Kolics et al., who reported that in 0.1 M NaCl solution, pH below 4 causes a significant reduction in the nanometric alumina (Al_2O_3) layer on pure aluminum due to active metal dissolution and oxide film destabilization [38].

After 4 h of bacterial growth, the pH gradually increases reaching 7.25 by 18 h. This gradual increase in pH could be associated with the bacterial metabolism of organic acids in the solution, as more easily metabolizable nutrients begin to deplete. At 18 h of exposure, a pH increase was recorded, which reached a value of 8.1 after 40 h of growth. According to Neerincx et al., *P. aeruginosa* can produce hydrogen cyanide (HCN) as a competitive mechanism [39]. To prevent toxicity, this bacterium regulates the HCN concentration through enzymatic conversion to ammonia, which may explain the pH rise observed after 18 h of growth.

Therefore, initial pH decreases of MHCl medium with *P. aeruginosa*, along with the highly probable lower pH of the microenvironments near the bacterial colonies adhered to the surface, may compromise the protective properties of the aluminum oxide layer. This effect is particularly critical during the exponential growth stage, when bacterial metabolic activity reaches optimal conditions, contributing to microbiologically influenced corrosion (MIC) documented in this study.

3.2.3. *Open circuit potential measurement*

Fig. 2c illustrates the changes in open circuit potential (OCP) of the AA2060-T8 alloy in MHCl medium. For the samples immersed in sterile MHCl, the OCP increased to −0.831 V during the first 2 h, which was attributed to the interaction of the native aluminum oxide with the aqueous environment, leading to the formation of a passive aluminum oxide-hydroxide layer. Between 2 and 20 h, the OCP gradually increased to −0.788 V, suggesting the progressive development of the passive oxide layer. Subsequently, between 20 and 40 h, the OCP reached a plateau, indicating the dynamic steady state of the oxide-hydroxide layer.

For the AA2060-T8 samples immersed in MHCl with *P. aeruginosa*, a similar behavior during lag stage (0–2h) was observed, consistent with low bacterial activity and the weak biofilm formation capacity (Table 2). However, at 4 h of exposure to *P. aeruginosa*, a sharp increase in OCP was observed, coinciding with the exponential growth stage. After 4 h, the OCP continued to rise, beginning to stabilize around 24 h, coinciding with the stabilization of biofilm-forming capacity and the end of the exponential growth stage. Subsequently, the OCP gradually increased until 40 h, reaching a plateau when the specific biofilm-forming capacity stabilized at a constant value (SBF = 1.01).

The sharp increase at 4 h aligns with the findings of Armon et al., who reported an exponential increase in the adsorption kinetics of *Pseudomonas fluorescens* on the surface of AA5052 aluminum alloy after 4 h of exposure [40]. Consequently, this sharp OCP increase at 4 h could likely represent early bacterial adhesion through EPS production, forming initial colonies during the exponential growth stage. Furthermore, the observed OCP increase may have been influenced by oxygen (O_2) generation through the catalase-mediated decomposition of H_2O_2. In aerobic bacteria, metabolic processes continuously produce hydrogen peroxide (H_2O_2). Due to its cytotoxicity, these organisms synthesize enzymes such as catalase to decompose H_2O_2 into O_2. This mechanism has been demonstrated in three catalase-positive microorganisms: *Escherichia coli*, *Staphylococcus aureus* [41], as well as *P. aeruginosa* [42]. In the latter study, Javier et al. reported an increase in OCP values after 4 h of *P. aeruginosa* growth in Mueller-Hinton medium, which was attributed to O_2 production from catalase activity. Furthermore, they employed modified carbon electrodes to detect O_2 generated by enzymatic activity at different pH, reporting pronounced electrocatalytic activity of catalase at pH 7.5. This optimal pH aligns with the values observed during the exponential growth stage in this study (Fig. 2b). Based on this observation, it is plausible that the bacterium produced O_2 through the decomposition of H_2O_2 via catalase activity, which may have contributed to the increase in OCP observed during early stage.

Another important aspect to consider in OCP analysis is the *P. aeruginosa* biofilm composition, which is primarily composed of alginate, a polymer known for its insulating properties [33,43]. During the early exponential growth stage (3–10 h), an initial firmly adhered layer formed on the surface, as evidenced by the marked increase in OCP

at 4 h (Fig. 2c). However, biofilm-forming capacity increased in parallel with bacterial growth, reaching $SBF_{40h} = 1.01$, indicating strong biofilm formation (Table 2). Considering the horizontal positioning of the alloy at the bottom of the electrochemical cell, the strong biofilm formation of exopolysaccharide, produced by the suspended bacterial population, progressively settled onto the AA2060-T8 surface as the experiment progressed. This progressive accumulation of organic deposits could have potentially influenced the observed OCP increase. This is consistent with previous observations of organic film-induced positive OCP shifts on AA2060-T8 Al–Cu–Li surface [44]. Furthermore, Li et al. [45] reported a positive OCP shift on steel surfaces, attributed to biofilm formation by *P. aeruginosa*, suggesting a similar effect by biofilm accumulation.

Additional processes may also occur at the metal–biofilm interface—such as pH changes induced by acidic metabolites or localized corrosion driven by differential aeration cells, both discussed in other sections of this study. However, the results suggest that two main factors could contribute to the OCP increase: (1) oxygen (O_2) generation from the catalase-mediated decomposition of H_2O_2, and (2) the progressive accumulation of organic deposits on the AA2060-T8 alloy surface. These processes could act simultaneously, resulting in the positive OCP shift observed throughout the bacterial growth stages.

3.2.4. Potentiodynamic polarization

Potentiodynamic polarization curves in Fig. 3a reveal an anodic shift in the corrosion potential (E_{corr}) for the samples immersed during 40h in MHCl with *P. aeruginosa*. This shift aligns with the OCP trends (Fig. 2c), reflecting the influence of the firmly adhered biofilm on the Al–Cu–Li alloy surface. A plausible explanation for this positive shift may involve the presence of an organic layer firmly bound to the surface via metal–organic interactions from biofilm functional groups, as reported for *P. aeruginosa* biofilms on steel [33] and *Pseudomonas putida* biofilms on AA7075 aluminum alloy [15].

In addition, a pronounced increase in current was recorded after a few mV of anodic sweep for AA2060-T8 exposed to the MHCl with *P. aeruginosa*. This may be associated with the formation of acidic microenvironments beneath the biofilm, which can prevent the repassivation of the natural oxide film, making it prone to breakdown [37]. The impact of these microenvironments was evidenced by an increase in the corrosion currents, which reached values nearly four times higher than those observed in the sterile control (Table 3).

The increase in corrosion current ($\boldsymbol{I_{corr}}$) observed in samples exposed to MHCl with *P. aeruginosa* can be directly correlated with the corrosion rate ($\boldsymbol{v}$) using Faraday Equation (3), which incorporates the molar mass of the metal ($\boldsymbol{M}$), the number of electrons transferred ($\boldsymbol{n}$), Faraday's constant ($\boldsymbol{F}$), the material's density ($\boldsymbol{\rho}$), and the exposed area ($\boldsymbol{A}$).

$$v = \frac{M \cdot I_{corr}}{n \cdot F \cdot \rho \cdot A} \tag{3}$$

Consequently, the increase in I_{corr} for the AA2060-T8 alloy after 40 h suggests a higher corrosion rate in the MHCl medium with *P. aeruginosa*. It is important to note that, to obtain representative current values of the metal surface after 40 h of exposure to the culture medium, these measurements were performed under ex-situ conditions, removing the non-adherent biofilm from the metallic surface.

Despite the correlation between the current increase and accelerated corrosion, this parameter only reflects the average electrochemical behavior. Typically, *P. aeruginosa* biofilms are correlated with MIC by two main factors: (1) generating differential cells by local variations in dissolved O_2, Cl^-, or pH, accelerating the alloy damage beneath the biofilm, and (2) an insulating nature attributed to the production of EPS, such as alginate, which can mask localized phenomena and alter the exposed area (Equation (3)). Based on the increase in I_{corr} and pH changes observed in this study, the first MIC-related factor appeared to be more relevant. However, the exact contribution of each factor remains unclear. Additional studies using local electrochemical techniques such as SVET and SECM [46] could help clarify the specific roles of differential aeration effects and EPS-related insulation during the different stages of bacterial growth on Al–Cu–Li surfaces.

Furthermore, Fig. 3b shows the macroscopic effects on the AA2060-T8 alloy surface after 40 h of exposure to sterile MHCl medium and to *P. aeruginosa*, followed by ex-situ anodic sweeps at +0.4 V, which promoted corrosion sites at the macroscopic scale. For the AA2060-T8 sample exposed to MHCl sterile, the localized corrosion sites formed were more numerous but smaller in diameter. In contrast, the corrosion sites were significantly larger for the sample exposed to MHCl with *P. aeruginosa*. These sites, associated with severe localized corrosion, showed distinctive rings of corrosion products expelled during hydrogen

Table 3
E_{corr} and I_{corr} determined from the polarization curves of AA2060-T8 after 40 h of exposure to MHCl.

AA2060-T8 Sample	E_{corr} (V vs SCE)	I_{corr} (A/cm^2)
Sterile	−0.690 ± 0.016	(1.9 ± 0.8) x10^{-7}
With *P. aeruginosa*	−0.539 ± 0.026	(7.0 ± 1.8) x10^{-7}

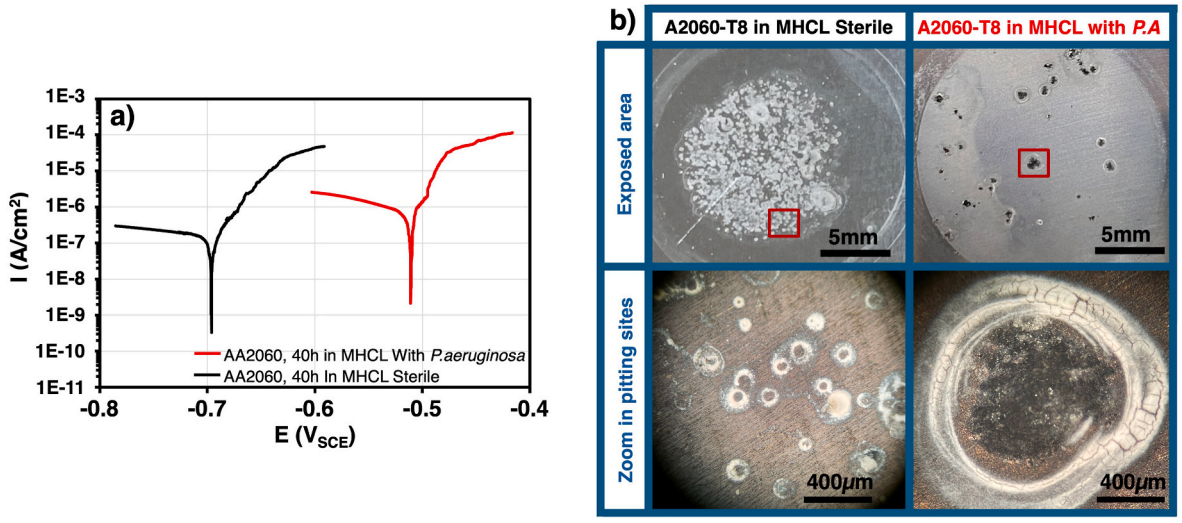

Fig. 3. (a) Potentiodynamic polarization curves of the AA2060-T8 alloy after 40 h of exposure to the MHCl medium. (b) AA2060-T8 alloy surface after 40 h of exposure to the MHCl medium, and subsequent potentiodynamic polarization up to +0.4V vs. OCP.

gas release from within the corrosion pits [47]. The increase in site diameter under bacterial conditions suggests that the AA2060-T8 surface becomes more susceptible to severe localized corrosion due to the influence of bacterial metabolism. To provide a more accurate representation of the number, depth and severity of the corroded regions influenced by bacterial activity, further studies will complement these findings with morphological and quantitative techniques, including weight loss measurements and profilometry.

3.3. Analysis of biofilm formed on AA2060-T8 alloy

3.3.1. Surface analysis

SEM-EDS analysis was performed on the alloy surface after immersion in MHCl with *P. aeruginosa* for 3, 10, and 24 h at 25 °C (Fig. 4).

After 3 h of exposure to the MHCl medium with *P. aeruginosa* (Fig. 4a), no visible bacteria were observed on the alloy, indicating that the biofilm was insufficient to support bacterial adhesion during the first hours of the exponential growth stage. However, after 10 h of exposure (Fig. 4b), the formation of a microbial colony adhering to the alloy surface through a biofilm was observed, corresponding to the midpoint of the exponential growth stage. These colonies, visible only after 10 h, consist of sessile, rod-shaped *P. aeruginosa* bacteria (2.1 μm in length) attached to the Al–Cu–Li alloy through the biofilm (Fig. 4d and 4e). This adhesion aligns with AFM studies on steel surfaces reported by Yuan and Pehkonen, who demonstrated that the morphology of *P. aeruginosa* adhered to surfaces via biofilm formation [48]. After 24 h, a mature biofilm on the surface was observed (Fig. 4c), indicating a heterogeneous biofilm structure formed during the stationary stage. Moreover, Fig. 4f shows the aluminum map, where local areas with a higher relative concentration of Al can be identified, which was associated with localized corrosion occurring beneath the biofilm. These findings are consistent with the specific biofilm formation (SBF) results (Fig. 2a, right axis) and the marked increase in OCP observed at 4 h, attributed to biofilm accumulation on the surface (Fig. 2c). Therefore, a colonization time range of 3–10 h was identified during the first half of the exponential growth stage. Within this range, *P. aeruginosa* produced a critical biofilm amount sufficient to sustain irreversible adhesion on the alloy surface, establishing a clear correlation between biofilm development and bacterial adhesion.

3.3.2. Cross-sectional analysis

To understand the MIC process beneath the biofilm, a cross-section analysis was conducted on the AA2060-T8 alloy after 24 h of immersion in MHCl with *P. aeruginosa* at 25 °C (Fig. 5).

The elemental mapping of carbon (Fig. 5c) primarily corresponds to the fixative resin, while the mappings of Al and Cu (Fig. 5e and 5 h) represent the principal alloying elements in the AA2060-T8 AlCuLi alloy. Consequently, as shown in Fig. 5a clearly shows the distinction between the epoxy resin used to fix the biofilm and the alloy.

One of the critical steps in this study was to distinguish between biofilm and corrosion products. The oxygen mapping (Fig. 5d) captured oxygen signals from both the corrosion products and the organic components of the biofilm. However, the phosphorus mapping (Fig. 5f) helped further clarify this distinction by highlighting the phosphorus-rich phospholipids present in both the bacterial cell membrane and the biofilm, thereby differentiating the aluminum corrosion products from the biofilm. It is important to note that a low carbon signal from the biofilm region does not indicate an absence of carbon. Instead, this is due to a contrast effect caused by the strong carbon signal from the fixative resin.

A localized decrease in Al intensity and an increase in O and Cl intensity were observed between the biofilm and the alloy (Fig. 5e, 5.d, and 5.g). Based on the observed composition of the corrosion products, which include Al, O, and Cl, it is suggested that the resulting compound

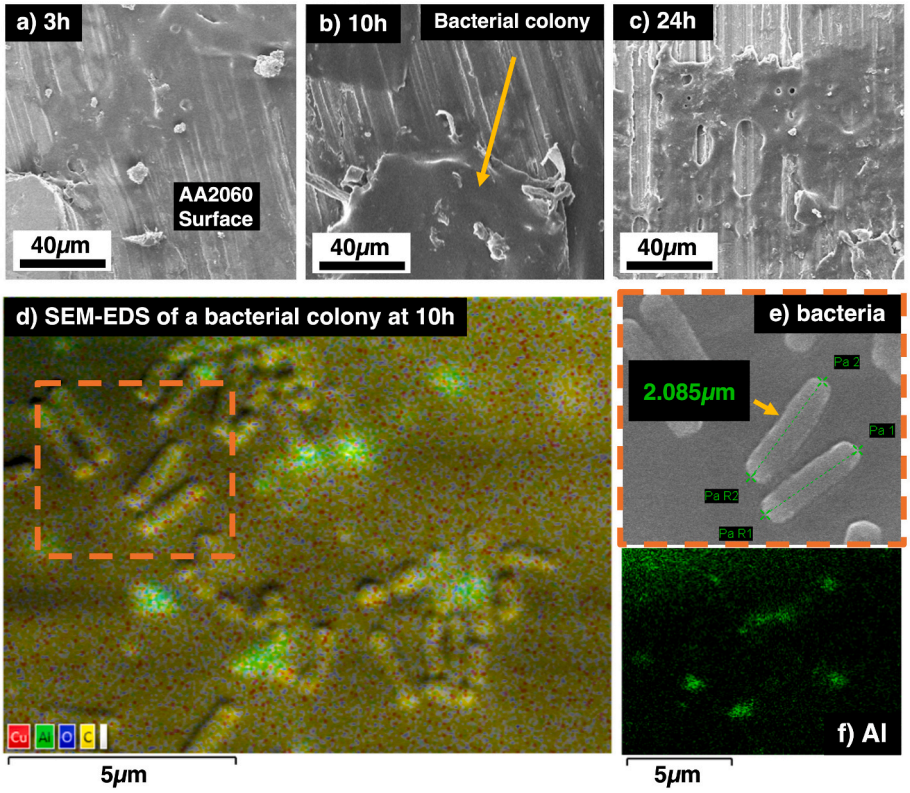

Fig. 4. The surface of AA2060-T8 after immersion in MHCl with *P. aeruginosa* at 25 °C, illustrating progressive changes during the biofilm formation process. (a) After 3 h of immersion, (b) after 10 h, (c) after 24 h, (d) SEM-EDS analysis of a bacterial colony at 10 h, (e) close-up view of the bacteria, and (f) Al mapping on a bacterial colony.

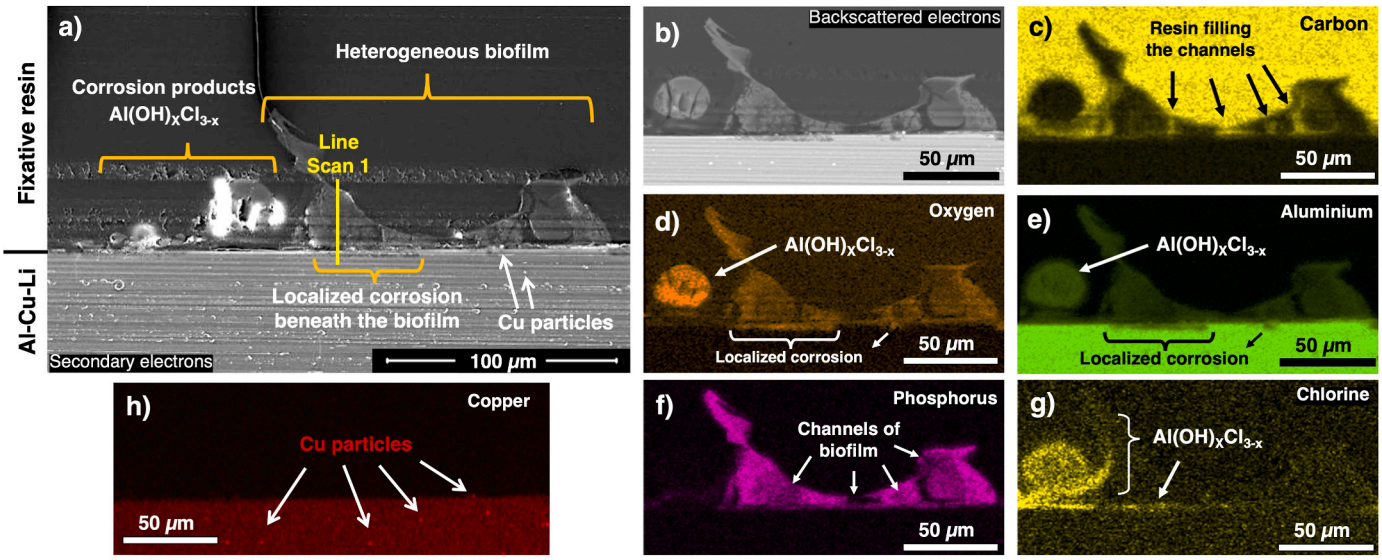

Fig. 5. Cross-sectional SEM-EDS analysis of the AA2060-T8 alloy with a heterogeneous biofilm adhered to the surface after 24 h of bacterial growth.

could correspond to $Al(OH)_XCl_{3-X}$, typically formed during the localized corrosion process in chloride solutions [49]. Moreover, Fig. 5g shows the presence of Cl beneath the biofilm, suggesting that $Al(OH)_XCl_{3-X}$ compounds could have formed both at the edges and beneath the biofilm. This indicates that the Cl-rich MHCl medium could have penetrated the biofilm and reached the alloy surface, thereby promoting localized corrosion. For this process to occur beneath the biofilm, anodic and cathodic reactions must proceed simultaneously.

$$\text{Anodic reaction}: Al \leftrightarrow Al^{3+} + 3e^- \quad (4)$$

$$\text{Hydrolysis reaction}: Al^{3+} + 3H_2O \leftrightarrow Al(OH)_3 + 3H^+ \quad (5)$$

$$\text{Cathodic reactions}: 2H_2O + O_2 + 4e^- \leftrightarrow 4OH^- \text{ or } 2H^+ + 2e^- \leftrightarrow H_2 \quad (6)$$

Once the alloy is introduced into the MHCl medium, the native alumina (Al_2O_3) reacts with water to form boehmite (AlO(OH)). During the exposure to the MHCl medium, soluble complexes form between aluminum oxides-hydroxides and chloride ions, destabilizing the passive layer [49]. Consequently, localized corrosion is initiates at weak points in the native oxide-hydroxide film, exposing the alloy to the MHCl medium [50]. In these exposed zones (anodic region), the formed Al^{3+} ions (Equation (4)) reacted immediately with water, leading to the formation of aluminum hydroxides (Equation (5)). Meanwhile, the cathodic region, located on the Cu particles at the interface between the Al–Cu–Li surface and the adhered biofilm (Fig. 5h), facilitates reduction reactions (Equation (6)), thus completing the electrochemical circuit [18]. Fig. 6 presents a line scan of this Cl-rich region under biofilm.

In Fig. 6, different layers of the transverse cut are identified. From left to right, the base metal is followed by the $Al(OH)_XCl_{3-X}$ layer (characterized by Al, O, and Cl signals), the biofilm adhered to the surface (identified by P and O signals), and finally the fixative resin, distinguished by an increase in C signals and a decrease in all other signals.

A critical factor contributing to the biofilm adhesion observed in Fig. 6 is alginate, the primary EPS produced by *P. aeruginosa* [43]. Alginate is a linear copolymer of alternating guluronic and mannuronic acid units, known for its ability to coordinate with metal centers through its carbonyl groups [33]. Recently, Gómez et al. detected, via FT-IR, interactions between carboxylate groups from alginate (produced by *Pseudomonas putida*) and the AA7075-T6 alloy surface, promoting the direct bonding of biofilms to the alloy surface and enhancing adhesion [15]. On this basis, if this interaction were primarily between alginate and the metal surface, aluminum would be concentrated near the metal surface, progressively decreasing within the biofilm as the distance from the surface increases. However, the aluminum intensity measured across the biofilm (Fig. 6) remains relatively constant at 10K–20K counts per second, indicating that the aluminum concentration in the biofilm did

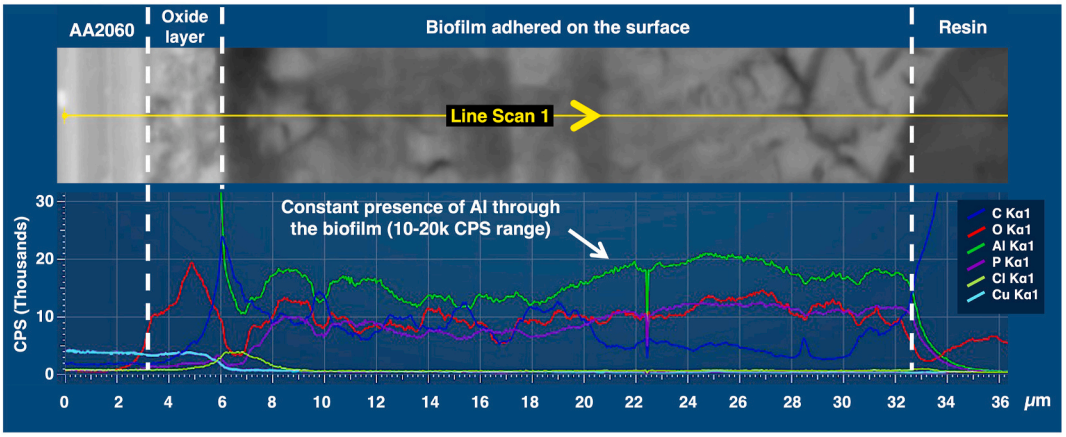

Fig. 6. Elemental Line Scan N°1, as depicted in Fig. 5, showing the elemental distribution across the biofilm adhered to the Al–Cu–Li alloy.

not decrease as the distance from the surface increases. Given the acidic nature of the carboxyl groups of alginate, those present in the *P. aeruginosa* biofilm became progressively deprotonated as the pH increased, reaching 8.1 after 40 h (Fig. 2b). At this stage, the carboxylic groups of alginate were predominantly deprotonated and negatively charged, making them available to interact with positively charged aluminum compounds formed during the corrosion process.

Therefore, based on the constant presence of aluminum on the transversal section of biofilm and the deprotonated carboxylate groups by pH increase during bacterial growth, an alternative interpretation of the biofilm's role in the MIC process is proposed. In addition to improving adhesion, carboxylate groups may chelate aluminum-based corrosion products dissolved in the medium, removing them from the system. According to Le Chatelier principle, this removal would shift the anodic reaction equilibrium (Equation (4)) towards product formation, acting as a driving force to further metal dissolution, thereby accelerating the corrosion process of the AA2060-T8 alloy during the biofilm forming process.

3.3.3. *Close-up on biofilm channels*

As discussed in the previous sections, biocorrosion is a highly complex process involving several factors such as metabolic activity, pH changes, and biofilm formation. It is generally agreed that biofilm formation occurs in three stages: 1) planktonic cells initiate adhesion on a metal surface, 2) establishment of bacterial colonies on the surface through the production of EPS, and 3) formation of a mature biofilm and its spread colonies over the surface. In this final stage, the presence of microbial cells on the metal surface, along with their metabolic activities, alters electrochemical processes, leading to the formation of localized cathodes or anodes. However, direct evidence explaining how these zones form beneath the biofilm remains unclear. To understand the differential cell phenomena in our samples, close-up elemental mapping was performed on a localized corrosion region beneath the biofilm (Fig. 7).

The EDS analysis revealed localized discontinuities within the biofilm, where the intensity of Al, O, and P signals decreases (Fig. 7d, 7.e, 7.f) while the carbon intensity increased (Fig. 7c). This suggests that resin carbon infiltrated these biofilm discontinuities, confirming the heterogeneity of the biofilm as it did not adhere uniformly to the surface. Directly beneath these discontinuities, localized corrosion products were identified adjacent to a Cu-rich particle (Fig. 7a). This localized corrosion phenomenon has been previously reported in the AA2198-T8 Al–Cu–Li alloy as a microscopic galvanic corrosion mechanism between Cu-rich particles and the Al-matrix [51]. This mechanism is particularly prevalent in T8 heat-treated alloys, such as AA2060-T8, due to the formation of deformed grains with a higher density of the T1 phase, which selectively dissolves and leads to localized corrosion. A line scan was performed on this localized corrosion area (Fig. 8).

The line scan in Fig. 8 shows a region between 6 and 8.6 μm where a maximum carbon signal was detected at 7 μm. However, the oxygen and phosphorus signals were very low, suggesting the absence of biofilm within this range. Based on these results, the carbon signal suggests that the resin partially filled this site, which was associated with pitting corrosion, as observed in Fig. 7b. Between 8.6 and 12 μm, the carbon signal decreases to the same level as phosphorus and oxygen, both of which increase slightly, which was associated with a thin organic layer remaining over the pitting corrosion site. Beyond 12 μm, all intensities dropped to nearly zero, except for carbon, which increases, indicating that the region above the localized corrosion was filled with epoxy resin. These discontinuities, formed during the biofilm formation process, likely served as channels during the bacterial growth stages, facilitating the transport of nutrients from the MHCl medium to the colonies adhered to the AA2060-T8 alloy surface. As a result, these channels exposed the surface to Cl^- ions and the pH fluctuations measured during the biofilm formation period, closing the galvanic circuit between the Cu-rich particles and the aluminum matrix, thereby triggering localized corrosion. Furthermore, the presence of these channels suggests the formation of oxygen concentration cells beneath the biofilm. Further studies could adopt the microscale spatial approach proposed by Klementiev et al. [52] to map oxygen concentration directly over the channels present in *P. aeruginosa* biofilms, thereby expanding the understanding of MIC mechanisms in Al–Cu–Li alloys.

Fig. 9 summarizes the results of this study. During the first hour of exposure, the interaction of the native aluminum oxide with the aqueous environment leads to the formation of a passive aluminum oxide hydroxide layer. Between 3 and 10 h, an initial heterogeneous biofilm

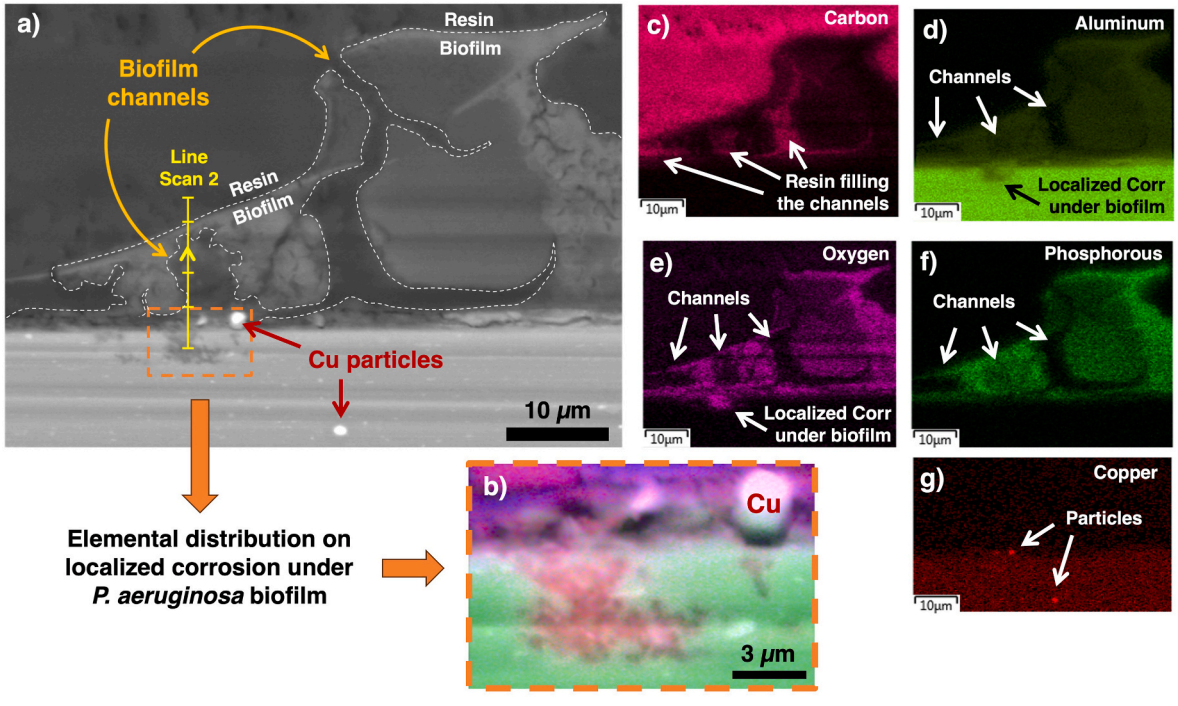

Fig. 7. Cross-sectional SEM-EDS analysis of AA2060-T8 (close-up from Fig. 5): evidence of localized corrosion beneath the biofilm and biofilm channels.

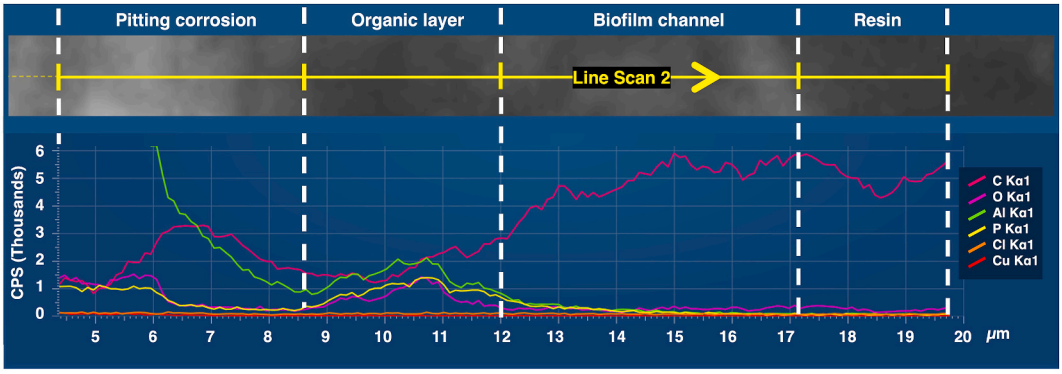

Fig. 8. Elemental Line Scan N°2, as depicted in Fig. 7, showing the elemental distribution across the biofilm channel.

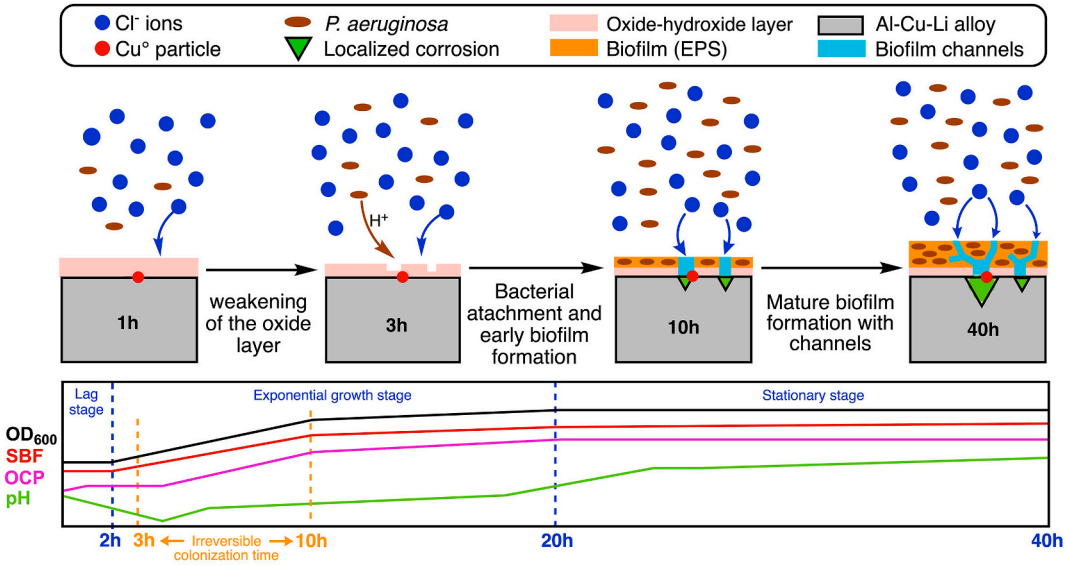

Fig. 9. Chronological scheme of AA2060-T8 Al–Cu–Li Alloy surface during *P. aeruginosa* growth stages and biofilm formation.

forms on the Al–Cu–Li surface, accompanied by a decrease in the pH of the MHCl medium with *P. aeruginosa* at 4 h of growth. The acidic environment (~pH 3.5–4.5) reported within the core of *P. aeruginosa* colonies [14] can dissolve the aluminum oxide layer on AA2060-T8 [38], potentially facilitating pitting corrosion beneath the biofilm by prematurely destabilizing the passive layer, exposing the alloy to chloride attack during biofilm formation. Finally, the channels formed through the biofilm promote the establishment of local differential cells, thereby inducing localized corrosion beneath the biofilm. Based on these experimental results, the MIC process in the AA2060-T8 Al–Cu–Li alloy was driven by the combined effects of pH decrease and the formation of biofilm channels. Furthermore, ongoing research in our group aims to investigate the role of organic compounds produced by *P. aeruginosa* in corrosion mechanisms, as well as the correlation between local pH changes induced by bacterial activity and the behavior of the lithium-rich T1 phase during corrosion processes. This work constitutes the first reported case of microbiologically influenced corrosion (MIC) in Al–Cu–Li alloys, paving the way for future protection strategies and broader applications in the aerospace industry in the coming decades.

4. Conclusions

Key parameters such as OD_{600}, SBF, pH, and OCP were measured and correlated with the three stages of bacterial growth and biofilm formation on the AA2060-T8 alloy, demonstrating that *P. aeruginosa* biofilm can adhere to and grow on the alloy. A colonization time range of 3–10 h was identified, during which *P. aeruginosa* produces a critical amount of biofilm that was sufficient to sustain irreversible adhesion on the alloy surface. The pH decrease, attributed to organic acid production during the exponential growth stage, could have created conditions for oxide layer destabilization beneath the biofilm, making the alloy more susceptible to localized corrosion. Cross-sectional analysis of the alloy after 24 h of MIC testing revealed the heterogeneity of the biofilm, specifically the presence of discontinuities within the biofilm that directly exposed the alloy surface to the electrolyte medium. These results provide direct evidence of the localized corrosion induced by the differential zones beneath the biofilm formed on the AA2060-T8 Al–Cu–Li alloy. Therefore, the MIC process in the AA2060-T8 Al–Cu–Li alloy is driven by the combined effects of the pH decrease and the formation of biofilm channels, leading to increased corrosion currents after 40 h of exposure to the MHCl medium with *P. aeruginosa*.

Author contributions

Conceptualization of this study, C.G. Ramírez; methodology, C.G. Ramírez., M.I. Azócar; validation, C.G. Ramírez, M.I. Azócar, M. Páez, N. Vejar; investigation and formal analysis, C.G. Ramírez, M.I. Azócar, J. Araujo; Data curation, C.G. Ramírez, M.I, Azócar, C. Montero; writing – original draft: C.G. Ramírez, V. Jiménez. Review & editing: C.G. Ramírez, A. Monsalve, C. Montero, J. Espinoza, J. Araujo, N. Vejar, M.

Azócar, M. Gulppi, M. Páez, V. Jiménez, X. Zhou; funding acquisition, C. G. Ramírez; resources, M.I. Azócar, M. Páez, A. Monsalve, X. Zhou.

Declaration of generative AI technologies in the writing process

During the preparation of this work, the author(s) used GPT-4o to refine the language and improve clarity of the text. After using this tool, the author(s) reviewed and edited the content as needed and take(s) full responsibility for the content of the publication.

Declaration of competing interest

The authors declare the following financial interests/personal relationships which may be considered as potential competing interests: Cristian Gino Ramirez reports financial support was provided by Agencia Nacional de Investigación y Desarrollo de Chile. If there are other authors, they declare that they have no known competing financial interests or personal relationships that could have appeared to influence the work reported in this paper.

Acknowledgments

Cristián Gino Ramírez is grateful for the doctoral financial support (Grant No. 21201969) and doctoral internship (Grant No. 752230171) provided by the Agencia Nacional de Investigación y Desarrollo (ANID-Chile). Acknowledgments are extended to Professor Xiaorong Zhou for his support and for providing access to the University of Manchester's resources. In addition, Víctor M. Jiménez-Arévalo is grateful for the support of the Vicerrectoría de Investigación, Innovación y Creación through the postdoctoral project DICYT N° 022442 PC. Dr. Azócar thanks ANID for its financial support (FONDECYT N° 1240869).

References

[1] Dursun T, Soutis C. Recent developments in advanced aircraft aluminium alloys. Mat & Des 2014;56:862–71. https://doi.org/10.1016/j.matdes.2013.12.002.
[2] Gangi F, Mustilli M, Daniele LM, Coscia M. The sustainable development of the aerospace industry: drivers and impact of corporate environmental responsibility. Bus Strat Environ 2022;31(1):218–35. https://doi.org/10.1002/bse.2883.
[3] Li SS, Yue X, Li QY, Peng HL, Dong BX, Liu TS, et al. Development and applications of aluminum alloys for aerospace industry. J Mater Res Technol 2023;27:944–83. https://doi.org/10.1016/j.jmrt.2023.09.274.
[4] Proton V, Alexis J, Andrieu E, Delfosse JÖ, Deschamps A, De Geuser F, et al. The influence of artificial ageing on the corrosion behaviour of a 2050 aluminium-copper-lithium alloy. Corros Sci 2014;80:494–502. https://doi.org/10.1016/j.corsci.2013.11.060.
[5] Abd El-Aty A, Xu Y, Guo X, Zhang SH, Ma Y, Chen D. Strengthening mechanisms, deformation behavior, and anisotropic mechanical properties of Al-Li alloys: a review. J Adv Res 2018;10:49–67. https://doi.org/10.1016/j.jare.2017.12.004.
[6] Liu D jun, Tian G, Jin G feng, Zhang W, Zhang Y hong. Characterization of localized corrosion pathways in 2195-T8 Al–Li alloys exposed to acidic solution. Defence Technol 2023;25:152–65. https://doi.org/10.1016/j.dt.2022.05.004.
[7] Xiao G, An R, Yang J, Ma J. Research progress of new generation of aluminum–lithium alloys alloying. Adv Eng Mater 2024;26(12). https://doi.org/10.1002/adem.202301639.
[8] Lin Y, Lu C, Wei C, Zheng Z. Effect of aging treatment on microstructures, tensile properties and intergranular corrosion behavior of Al–Cu–Li alloy. Mater Char 2018;141:163–8. https://doi.org/10.1016/j.matchar.2018.04.043.
[9] Huang J, Feng S, Li S, Wu C, Chen J. The crystallographic corrosion and its microstructure in an Al-Cu-Li alloy. J Alloys Compd 2021;861. https://doi.org/10.1016/j.jallcom.2020.158588.
[10] Jiang Y, Xi J, Du L, Lei W, Xing J, Liu C, et al. Time-varying electrochemically heterogeneous entities during the micro-galvanic corrosion associated with nanoscale precipitates in an Al-Cu-Li alloy. Corros Sci 2022;206. https://doi.org/10.1016/j.corsci.2022.110542.
[11] Little BJ, Hinks J, Blackwood DJ. Microbially influenced corrosion: towards an interdisciplinary perspective on mechanisms. Int Biodeterior Biodegrad 2020;154. https://doi.org/10.1016/j.ibiod.2020.105062.
[12] Jia R, Unsal T, Xu D, Lekbach Y, Gu T. Microbiologically influenced corrosion and current mitigation strategies: a state of the art review. Int Biodeterior Biodegrad 2019;137:42–58. https://doi.org/10.1016/j.ibiod.2018.11.007.
[13] Chugh B, Sheetal Singh M, Thakur S, Pani B, Singh AK, et al. Extracellular electron transfer by *Pseudomonas aeruginosa* in biocorrosion: a review. ACS Biomater Sci Eng 2022;8:1049–59.
[14] Hollmann B, Perkins M, Chauhan VM, Aylott JW, Hardie KR. Fluorescent nanosensors reveal dynamic pH gradients during biofilm formation. NPJ Biofilms Microbiomes 2021;7. https://doi.org/10.1038/s41522-021-00221-8.
[15] Gómez-Bolívar J, Warburton MP, Mumford AD, Mujica-Alarcón JF, Anguilano L, Onwukwe U, et al. Spectroscopic and microscopic characterization of microbial biofouling on aircraft fuel tanks. Langmuir 2024;40(7):3429–39. https://doi.org/10.1021/acs.langmuir.3c02803.
[16] Smirnov VF, Belov DV, Sokolova TN, Kuzina OV, Kartashov VR. Microbiological corrosion of aluminum alloys. Appl Biochem Microbiol 2008;44:192–6. https://doi.org/10.1134/s0003683808020117.
[17] González EA, Leiva N, Vejar N, Sancy M, Gulppi M, Azócar MI, et al. Sol-gel coatings doped with encapsulated silver nanoparticles: inhibition of biocorrosion on 2024-T3 aluminum alloy promoted by *Pseudomonas aeruginosa*. J Mater Res Technol 2019;8(2):1809–18. https://doi.org/10.1016/j.jmrt.2018.12.011.
[18] Vejar N, Orrego M, Sancy M, Páez M. Microbiologically influenced corrosion in aluminium alloys 7075 and 2024. Aluminium alloys - Recent trends in processing, Characterization, mechanical behavior and applications. InTech; 2017. https://doi.org/10.5772/intechopen.70735.
[19] Zea L, Nisar Z, Rubin P, Cortesão M, Luo J, McBride SA, et al. Design of a spaceflight biofilm experiment. Acta Astronaut 2018;148:294–300. https://doi.org/10.1016/j.actaastro.2018.04.039.
[20] Rcheulishvili N, Zhang Y, Papukashvili D, Deng YL. Survey and evaluation of spacecraft-associated aluminum-Degrading microbes and their rapid identification methods. Astrobiology 2020;20(8):925–34. https://doi.org/10.1089/ast.2019.2078.
[21] Wu W, Jin Y, Bai F, Jin S. Pseudomonas aeruginosa. In: Yi WT, Sussman M, editors. Molecular Medical Microbiology. Elsevier; 2014. p. 753–67. https://doi.org/10.1016/B978-0-12-397169-2.00041-X.
[22] Pal MK, Lavanya M. Microbial influenced corrosion: understanding Bioadhesion and Biofilm Formation. J Bio Tribo Corros 2022;8. https://doi.org/10.1007/s40735-022-00677-x.
[23] Alasvand Zarasvand K, Rai VR. Microorganisms: Induction and inhibition of corrosion in metals. Int Biodeterior Biodegrad 2014;87:66–74. https://doi.org/10.1016/j.ibiod.2013.10.023.
[24] Vejar N, Gutiérrez S, Tareelap N, Alvarado C, Solís R, Guerra C, et al. Influence of Bacillus safensis and Bacillus pumilus on the electrochemical behavior of 2024-T3 aluminum alloy. Bioelectrochemistry 2022;143. https://doi.org/10.1016/j.bioelechem.2021.107950.
[25] Long YMA, Zhou XR, Meng XM, Huang WJ, Liao Y, Chen XL, et al. Influence of thermomechanical treatments on localized corrosion susceptibility and propagation mechanism of AA2099 Al–Li alloy. Trans of Nonferrous Met Soc China 2016;26(6):1472–81. https://doi.org/10.1016/S1003-6326(16)64252-8.
[26] Allkja J, Bjarnsholt T, Coenye T, Cos P, Fallarero A, Harrison JJ, et al. Minimum information guideline for spectrophotometric and fluorometric methods to assess biofilm formation in microplates. Biofilm 2020;2. https://doi.org/10.1016/j.bioflm.2019.100010.
[27] Niu C, Gilbert ES. Colorimetric method for identifying plant essential oil components that affect biofilm formation and structure. Appl Environ Microbiol 2004;70:6951–6. https://doi.org/10.1128/AEM.70.12.6951-6956.2004.
[28] Huang JY, Ming WQ, Wu CL. Effect of microstructure on corrosion behaviour of Al-Cu-Li alloys. Mater Char 2022;194. https://doi.org/10.1016/j.matchar.2022.112416.
[29] Yang Y, He G, Liu Y, Li K, Wu W, Huang C. Quantitative contribution of T1 phase to the strength of Al-Cu-Li alloys. J Mater Sci 2021;56:18368–90. https://doi.org/10.1007/s10853-021-06432-w.
[30] Li M, Seyeux A, Wiame F, Marcus P, Światowska J. Localized corrosion induced surface modifications of Al-Cu-Li alloy studied by ToF-SIMS 3D imaging. npj Mater Degrad 2021;5:23. https://doi.org/10.1038/s41529-021-00170-9.
[31] Ammar Y, Swailes D, Bridgens B, Chen J. Influence of surface roughness on the initial formation of biofilm. Surf Coat Technol 2015;284:410–6. https://doi.org/10.1016/j.surfcoat.2015.07.062.
[32] Zhang X, Zhou X, Ma Y, Thompson GE, Luo C, Sun Z, et al. The propagation of localized corrosion in Al-Cu-Li alloy. Surf and Interface Analysis, vol. 48. John Wiley and Sons Ltd; 2016. p. 745–9. https://doi.org/10.1002/sia.5890.
[33] Abdolahi A, Hamzah E, Ibrahim Z, Hashim S. Microbially influenced corrosion of steels by *Pseudomonas aeruginosa*. Corrosion Rev 2014;32:129–41. https://doi.org/10.1515/corrrev-2013-0047.
[34] Pellé J, Longo M, Le Poul N, Hellio C, Rioual S, Lescop B. Electrochemical monitoring of the *Pseudomonas aeruginosa* growth and the formation of a biofilm in TSB media. Bioelectrochemistry 2023;150. https://doi.org/10.1016/j.bioelechem.2022.108344.
[35] Naves P, Del Prado G, Huelves L, Gracia M, Ruiz V, Blanco J, et al. Measurement of biofilm formation by clinical isolates of Escherichia coli is method-dependent. J Appl Microbiol 2008;105:585–90. https://doi.org/10.1111/j.1365-2672.2008.03791.x.
[36] Deltombe E. Marcel Pourbaix. The electrochemical behavior of aluminum-potential pH diagram of the system Al-H_2O at 25 C. Corrosion 1958;14(11):16–20. https://doi.org/10.5006/0010-9312-14.11.16.
[37] Ghanbari E, Saatchi A, Lei X, Macdonald DD. Studies on pitting corrosion of Al-Cu-Li alloys Part II: breakdown potential and pit initiation. Materials 2019;12(11). https://doi.org/10.3390/ma12111786.
[38] Kolics A, Besing AS, Baradlai P, Haasch R, Wieckowski A. Effect of pH on thickness and ion content of the oxide film on aluminum in NaCl media. J Electrochem Soc 2001;148:B251. https://doi.org/10.1149/1.1376118.
[39] Neerincx AH, Mandon J, Van Ingen J, Arslanov DD, Mouton JW, Harren FJM, et al. Real-time monitoring of hydrogen cyanide (HCN) and ammonia (NH_3) emitted by

Pseudomonas aeruginosa. J Breath Res 2015;9. https://doi.org/10.1088/1752-7155/9/2/027102.

[40] Armon R, Starosvetsky J, Dancygier M. Adsorption of flavobacterium breve and pseudomonas fluorescens P17 on different metals: electrochemical polarization effect. Biofouling 2001;17:289–301. https://doi.org/10.1080/08927010109378489.

[41] Gulppi M, Muñoz L, Vejar N, Blamey JM, Gonzalez E, Azócar M, et al. Electrochemical dynamic sensing of hydrogen peroxide in the presence of microorganisms. Electrochim Acta 2019;305:416–22. https://doi.org/10.1016/j.electacta.2019.03.076.

[42] Espinoza-Vergara J, Molina P, Walter M, Gulppi M, Vejar N, Melo F, et al. Effect of pH on the electrochemical behavior of hydrogen peroxide in the presence of *Pseudomonas aeruginosa*. Front Bioeng Biotechnol 2021;9. https://doi.org/10.3389/fbioe.2021.749057.

[43] Reichhardt C, Parsek MR. Confocal laser scanning microscopy for analysis of *Pseudomonas aeruginosa* biofilm architecture and matrix localization. Front Microbiol 2019;10. https://doi.org/10.3389/fmicb.2019.00677.

[44] Espinoza-Vergara J, Gad S, Silva CP, Paez MA, Jin Z, Xiong Y, et al. Covalent electrografting of aryl groups on AA2060-T8 surfaces, and their modification with Ce(4OHcin)3 to incorporate additional anticorrosive activity. J Mater Res Technol 2024;31:3014–24. https://doi.org/10.1016/j.jmrt.2024.07.009.

[45] Li H, Zhou E, Zhang D, Xu D, Xia J, Yang C, et al. Microbiologically influenced corrosion of 2707 Hyper-duplex stainless steel by marine *Pseudomonas aeruginosa* biofilm. Sci Rep 2016;6. https://doi.org/10.1038/srep20190.

[46] Chang W, Qian H, Li Z, Mol A, Zhang D. Application and prospect of localized electrochemical techniques for microbiologically influenced corrosion: a review. Corros Sci 2024;236. https://doi.org/10.1016/j.corsci.2024.112246.

[47] Ma Y, Zhou X, Huang W, Thompson GE, Zhang X, Luo C, et al. Localized corrosion in AA2099-T83 aluminum-lithium alloy: the role of intermetallic particles. M Chem Phys 2015;161:201–10. https://doi.org/10.1016/j.matchemphys.2015.05.037.

[48] Yuan SJ, Pehkonen SO. AFM study of microbial colonization and its deleterious effect on 304 stainless steel by *Pseudomonas* NCIMB 2021 and *Desulfovibrio desulfuricans* in simulated seawater. Corros Sci 2009;51(6):1372–85. https://doi.org/10.1016/j.corsci.2009.03.037.

[49] McCafferty E. Sequence of steps in the pitting of aluminum by chloride ions. Corros Sci 2003;45(7):1421–38. https://doi.org/10.1016/S0010-938X(02)00231-7.

[50] Ghali E. Aluminum and aluminum alloys. In: Revie RW, Uhlig H, editors. Uhlig's corrosion handbook. third ed. Hoboken (NJ): John Wiley & Sons; 2011. p. 730.

[51] de Sousa Araujo JV, Santos Bugarin A, de F, Donatus U, Machado C de SC, Queiroz FM, Terada M, et al. Thermomechanical treatment and corrosion resistance correlation in the AA2198 Al–Cu–Li alloy. Corr Eng Sci Technol 2019;54:575–86. https://doi.org/10.1080/1478422X.2019.1637077.

[52] Klementiev AD, Jin Z, Whiteley M. Micron scale spatial measurement of the o2 gradient surrounding a bacterial biofilm in real time. mBio 2020;11:1–7. https://doi.org/10.1128/mBio.02536-20.